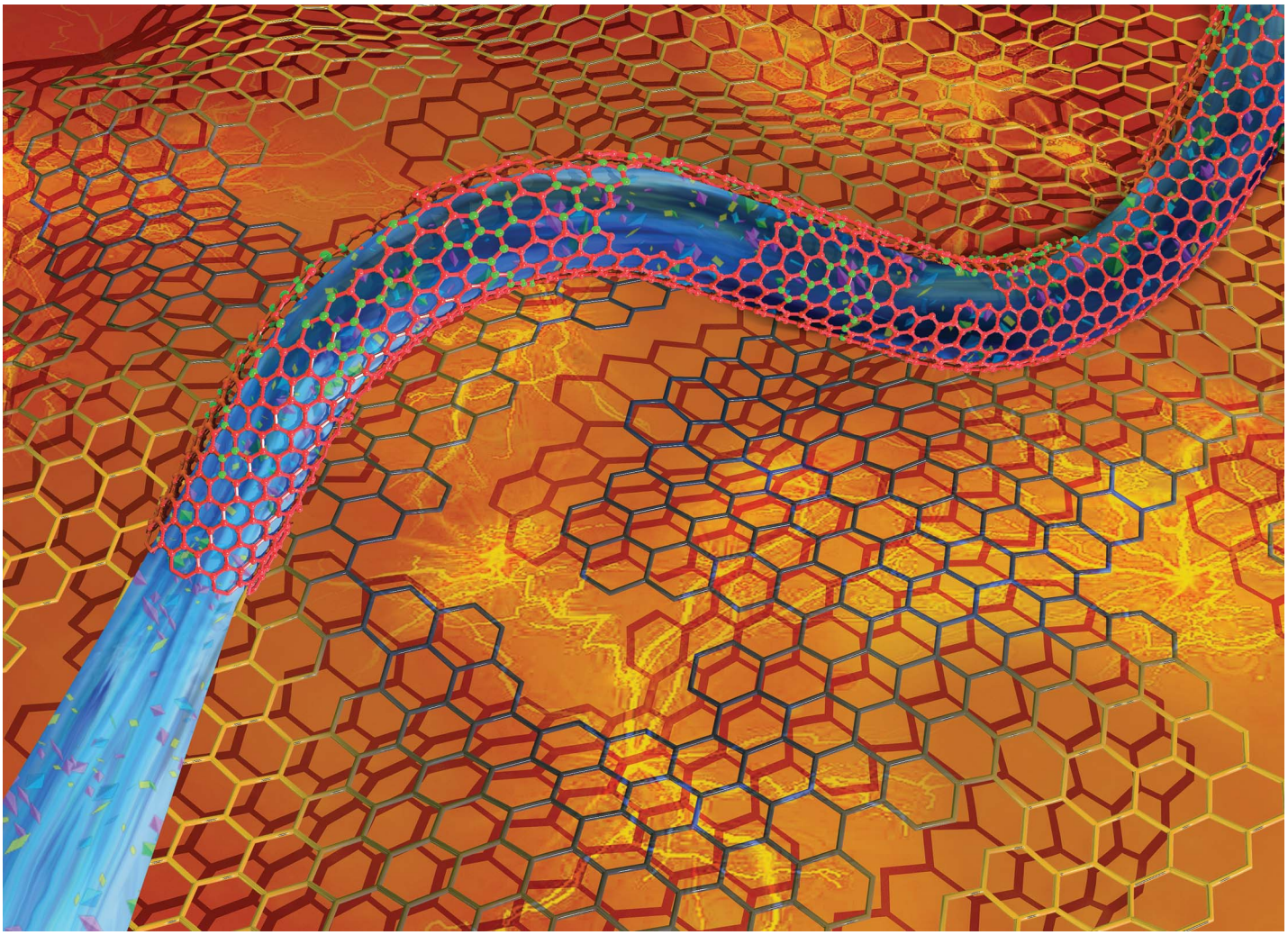

**Showcasing a study on the fabrication of a low-cost microfluidic bio-electricity production system with superior oxygen reduction reaction catalysis reported by Dr Yang Yang, Prof. Dingding Ye, Prof. Xun Zhu and Prof. Qiang Liao at Chongqing University, and Prof. Yat Li at the University of California, Santa Cruz.**

A three-dimensional nitrogen-doped graphene aerogel-activated carbon composite catalyst that enables low-cost microfluidic microbial fuel cells with superior performance

A novel nitrogen-doped graphene aerogel blended with activated carbon serves as the oxygen reduction reaction catalyst to lower the fabrication cost. An air-breathing microfluidic-controlled microbial fuel cell based on this catalyst delivers a remarkably high power density and could be potentially constructed as a self-powered bio-sensor or as a power source for an on-line total analysis system.

## As featured in:

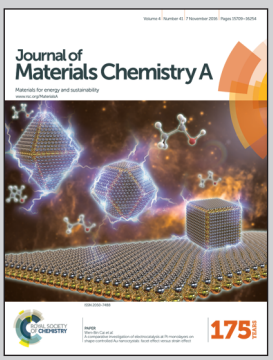


See Dingding Ye, Yat Li *et al.*, *J. Mater. Chem. A*, 2016, **4**, 15913.

ROYAL SOCIETY OF CHEMISTRY

www.rsc.org/MaterialsA

Registered charity number: 207890

Journal of Materials Chemistry A

PAPER

View Article Online
View Journal | View Issue



Cite this: J. Mater. Chem. A, 2016, 4, 15913

# A three-dimensional nitrogen-doped graphene aerogel-activated carbon composite catalyst that enables low-cost microfluidic microbial fuel cells with superior performance†

Yang Yang,[ab] Tianyu Liu,[b] Qiang Liao,[a] Dingding Ye,*[a] Xun Zhu,[a] Jun Li,[a] Pengqing Zhang,[a] Yi Peng,[b] Shaowei Chen[b] and Yat Li*[b]

Received 15th June 2016
Accepted 10th August 2016

DOI: 10.1039/c6ta05002f

www.rsc.org/MaterialsA

Microfluidic microbial fuel cells (μMFCs) are promising miniaturized power generators and bio-sensors, which combine the micro-fabrication process with bio-chip technology. However, a limited power output and considerable cost severely restrict their practical applications. Previous research has revealed that inadequate colonization of bacteria on bio-anodes as well as sluggish oxygen reduction reaction (ORR) kinetics are two main causes for the unsatisfactory power output. In this study, we have demonstrated a μMFC that has successfully addressed the aforementioned limitations by utilizing low-cost self-assembled reduced graphene oxide–nickel (rGO@Ni) foam and a nitrogen-doped graphene aerogel-activated carbon (AC@N-GA) as the bio-anode and air-cathode electrodes, respectively. The three-dimensional and macro-porous structure of the rGO@Ni foam provides a large surface area for bacterial colonization and hence largely increases the loading amount of bacterial cells. The AC@N-GA electrode shows excellent ORR catalytic performance due to the meso-porous structure and the presence of nitrogen functionalities that can serve as the catalytic sites. As a result, the μMFC achieves a maximum power density of 1181.4 ± 135.6 W $m^{-3}$ (continuous-mode) and 690.2 ± 62.3 W $m^{-3}$ (batch-mode) evaluated based on the volume of the reactor (50 μL). To our knowledge, this is the highest volumetric power density reported for air-breathing μMFCs and microfluidic glucose fuel cells with a similar configuration. Besides, the utilization of the inexpensive electrodes and membrane-free architecture could significantly decrease the fabrication cost of μMFCs.

## Introduction

Microbial fuel cells (MFCs) are energy conversion devices that can convert chemical energy into bio-electricity *via* metabolic processes of exoelectrogens.[1,2] Among various scales of MFCs, the microfluidic MFCs (μMFCs) are emerging as promising power sources for some miniaturized electronics, *e.g.* bio-chips and bio-sensors, owing to their facile fabrication and small scale. Like other MFCs, a μMFC is composed of a microfluidic channel imbedded with a cathode and anode, and a piece of separator sandwiched between the two electrodes.[3,4]

However, two major limitations, the relatively low power output along with the considerable fabrication cost have severely hindered practicality of μMFCs. Previous studies confirmed that the insufficient bacterial growth on the bio-anode is the major cause for the unsatisfactory power output. To address this limitation, various strategies including optimization of microfluidic channel structures,[5,6] increasing the accessible surface area of conventional two-dimensional (2D) electrodes[7,8] and developing novel functional 2D materials[9–11] that can effectively facilitate and increase bacterial colonization have been extensively studied. Recently, graphene-based electrodes have shown promising performance in enhancing the anode performance of MFCs. Yuan *et al.* reported the combination of graphene-based bioanodes with air-cathodes to improve the power output of MFCs.[12] He *et al.* reported the preparation of chitosan–graphene bioanodes with abundant meso-/micro-pores.[13] A remarkably high power density of 1530 mW $m^{-2}$ was obtained, which was 78 times higher than that of conventional carbon cloth. The previous successes have inspired us to explore the use of graphene-based electrodes that can significantly improve the power output of μMFCs.

The high fabrication cost of μMFCs is related to the expensive components. Firstly, the use of ion-exchange membranes, *e.g.*, DuPont™ Nafion® 117 (~$3000 per 1 $m^2$) (Fuel Cells Etc.,

[a]Key Laboratory of Low-grade Energy Utilization Technologies and Systems (Chongqing University), Ministry of Education, Chongqing 400030, P. R. China. E-mail: dingdingye@cqu.edu.cn

[b]Department of Chemistry and Biochemistry, University of California, Santa Cruz, California 95060, USA. E-mail: yatli@ucsc.edu

† Electronic supplementary information (ESI) available. See DOI: 10.1039/c6ta05002f

US), is a major cost. Secondly, noble metal-based catalysts as oxygen reduction reaction (ORR) catalysts for the air-cathode are also costly parts. What's worse, the catalytic activity of some noble metal-based catalysts is not stable, which will drastically decrease the overall performance of μMFCs over a long period.[14] Most recently, graphene composites equipped with interconnected macro-porous frameworks have exhibited promising ORR catalytic performance and attracted much research attention as alternative ORR catalysts due to their low-cost.[15–17] Therefore, we believe utilization of graphene-based catalysts is crucial for reducing the overall cost of μMFCs.

In this study, we fabricated a membraneless μMFC with both graphene-based materials as the bio-anode and air-cathode. In particular, a piece of reduced graphene oxide-coated nickel foam (denoted as rGO@Ni) and nitrogen-doped graphene aerogel-supported activated carbon composite (denoted as AC@N-GA) serve as the bio-anode and air-cathode, respectively. The membrane-free configuration and inexpensive electrodes could greatly decrease the fabrication cost of our μMFC. Most importantly, the μMFC device achieved outstanding performance with a maximum volumetric power density of 1181.4 ± 135.6 W $m^{-3}$ (continuous-flow mode) and 690.2 ± 62.3 W $m^{-3}$ (batch-mode). These power densities are substantially higher than those of other μMFCs with a similar configuration. We ascribe the superior performance to the excellent ORR catalytic performance of AC@N-GA and the high surface area of rGO@Ni that can accommodate a large number of bacterial colonies for power generation.

# Experimental

### Preparation of electrode materials

The procedure for preparation of the electrodes was shown in Fig. S1, ESI.† Graphene oxide (GO) solution, the precursor of AC@N-GA, was prepared from oxidation and exfoliation of graphite (Fisher Science Education Inc., NJ) using a modified Hummer's method.[18,19] Briefly, graphite flakes (2.5 g) were mixed with 23 mL of concentrated $H_2SO_4$ (98 wt%) and 10 mL of concentrated $HNO_3$ (65 wt%) at 0 °C. After thoroughly mixing with two acids and gradually raising the temperature to 35 °C, 3 g of $KMnO_4$ was slowly poured into the mixture and mixed with the solution. After 3 h of mixing, the mixture was diluted with 40 mL of de-ionized water. After 12 h, the solution was further diluted by an additional 200 mL of deionized water and 3 mL of 30% $H_2O_2$. Once the reaction system cooled to room temperature, the GO powder was collected *via* centrifugation at 3000 rpm and washed with an ample amount of deionized water until the pH value of the rinse reached near 7. The GO solution was then dispersed in deionized water and vigorously sonicated to form a uniform suspension with a concentration of 5 mg $mL^{-1}$ (Fig. S1(a), ESI†). AC@N-GA was prepared by a reported hydrothermal method.[15] 8 mL of ammonium hydroxide (Fisher Scientific Inc., NJ) and 100 mg of activated carbon (AC) were subsequently added to 20 mL of the as-prepared GO dispersion. Then, the suspension was transferred into a Teflon liner and heated at 180 °C for 12 h to form the nitrogen-doped graphene-activated carbon composite hydrogel. The as-prepared composite hydrogel was lyophilized to obtain the composite aerogel (Fig. S1(b–d), ESI†). The sample was then annealed at 700 °C in an ammonia atmosphere for 3 h in a tube furnace. Finally, the product AC@N-GA was obtained.

The rGO@Ni anode was prepared by the following procedure. A piece of clean Ni foam was placed into a Teflon-lined autoclave and filled with the previously prepared GO solution. The autoclave was heated at 120 °C for 5 h and then cooled down to room temperature. The piece of Ni foam was taken out from the autoclave, washed with deionized (DI) water and then blow-dried by air. The Ni foam was uniformly deposited with black graphene layers after repeating the aforementioned deposition process three times.[19]

### Material characterization

The morphology of the electrode materials was probed with a scanning electron microscope (SEM, Hitachi S4800 II). The Brunauer–Emmett–Teller (BET) method using nitrogen adsorption/desorption at 77.3 K was performed to determine the specific surface area of the electrodes. Pore size distribution was characterized with a porosimetry analyzer (Micromeritics, ASAP 2020, USA) and analyzed according to the Barrett–Joyner–Halenda (BJH) adsorption model. The composition of AC@N-GA was measured by powder X-ray diffraction (XRD, Rigaku Americas Miniflex Plus powder diffractometer) and X-ray photoelectron spectroscopy (XPS, ESCALAB 250 Xi XPS System, and Al Kα radiation).

### Assembly and set-up of μMFCs

Fig. 1 presents a schematic illustration of the μMFC. The rGO@Ni and AC@N-GA were used as the bio-anode and air-cathode, respectively. A chamber with a dimension of 20 mm in length, 2.5 mm in width and 1 mm in height was engraved on a polymethylmethacrylate (PMMA) plate using a laser beam to serve as the microchannel. To test the performance of the μMFC in a continuous-mode operation, bacterial culture solution was continuously supplied into the microchannel with a syringe pump (Longer LSP02-1B, P. R. China) operated at pull-mode.

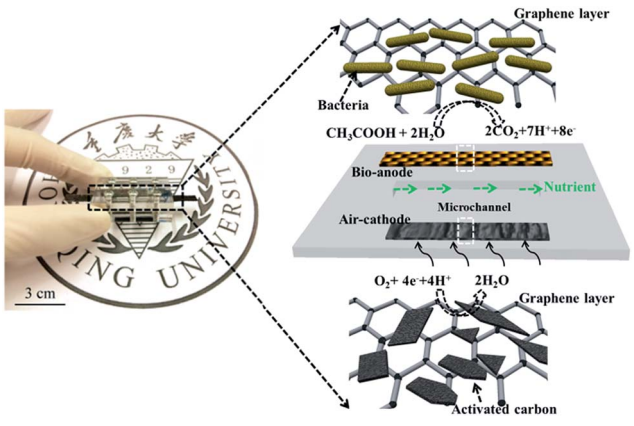


Fig. 1 Schematic illustration of the structure and working mechanism of the μMFC device.

Such a configuration enables a strong negative pressure inside of the μMFC that simultaneously sucks in oxygen gas and prevents leakage,[20] which does not need the help of the polytetrafluoroethylene layer. For the batch-mode operation, the μMFC was operated for 12 h in a cycle, and the entire electrolyte was replenished with fresh bacterial culture solution prior to another cycle. An Ag/AgCl (saturated KCl solution, +0.197 V *vs.* standard hydrogen electrode) was used as a reference electrode. All the experiments were carried out under ambient pressure and room temperature.

The μMFC was inoculated with anaerobic digester sludge containing exoelectrogenic bacteria. During the inoculation process, an external resistor of 5000 Ω was connected in series with the μMFC. The output voltage ($V$) across the external resistor was recorded using a digital multimeter (Model 34070A, Agilent Technologies Inc., CA). Once a fast voltage-increase was observed, a fresh medium containing 3.39 g $L^{-1}$ of sodium acetate (nutrients for bacteria), various inorganic salts (trace-elements for bacterial growth)[21] and phosphate buffer solution (18.2 g $K_2HPO_4$ and 2.45 g $KH_2PO_4$ dissolved in 1 L of deionized water) were injected to the microchannel.

### Electrochemical characterization

The catalytic performance of AC@N-GA was evaluated in a standard three-electrode cell connected to a CHI 710C electrochemical station (Chenhua Shanghai). A piece of platinum foil and an Ag/AgCl electrode were used as the counter and reference electrodes, respectively. The working electrode was a rotating (platinum) ring–(glassy carbon) disk electrode (RRDE). AC@N-GA paste was prepared by mixing 1 mg of AC@N-GA powder with 4 mg of carbon black (XC-72) and 10 μL of Nafion solution (Sigma-Aldrich Inc., MO), followed by ultrasonic mixing with 990 μL of ethanol. Then 10 μL of catalyst inks were pipetted dropwise onto the top of the disk electrode and air-dried. Prior to the measurement, 5 μL of 5 wt% Nafion solution was added onto the working electrode to ensure that the active material is firmly attached onto the glassy carbon. The oxygen-saturated 0.1 M KOH aqueous solution was used as the electrolyte.

The volumetric power density and polarization curves were obtained by varying the external resistances ($R$) from 100 kΩ to 1 kΩ. Voltages were recorded when the fluctuation was less than 2 mV (in 5 min). Current density ($I$) was calculated using the Ohm's law $I = V/R$, and power density ($P$) was calculated as $P = V \times I$. Both $I$ and $P$ were normalized to the volume of the microchannel (50 μL). All parameters of the cell performance test were collected in triplicate to ensure good reproducibility.

Electrochemical impedance spectroscopy (EIS) was conducted in a two-electrode testing system by an electrochemical workstation (Zahner, Germany). The spectrum was collected by combining the μMFC in series with an external resistor of 2000 Ω in a continuous-flow mode. The frequency was swept from 10 000 Hz to 0.01 Hz with a perturbation of 10 mV. The Nyquist plot was analyzed by fitting the spectra with an equivalent circuit (EC) by the ZSimpwin software.

## Results and discussion

Nitrogen-doped graphene aerogel (N-GA) has been demonstrated as a potential ORR catalyst in our previous study.[22] In order to further improve the ORR catalytic performance, low-cost commercially activated carbon pellets were combined with our N-GA to synthesize the activated carbon–N-GA composite (denoted as AC@N-GA). The AC@N-GA catalysts were prepared by adding 100 mg of activated carbon pellets into the N-GA precursor solution for the hydrothermal reaction (Experimental). The morphology and structure of the AC@N-GA electrodes were first determined by scanning electron microscopy (SEM) images and X-ray diffraction (XRD). As shown in Fig. 2a, the SEM image reveals that the AC@N-GA composite consists of an interconnected and hierarchically porous network structure with many activated carbon pellets embedded in the graphene matrix. The SEM image with large magnification (Fig. 2b) shows that the AC pellet has a very rough surface and is successfully anchored into the graphene matrix. The characteristic diffraction peak at 25°, which can be assigned to N-GA (Fig. 2e), is observed in the XRD spectrum of AC@N-GA as expected.[23]

The porous structure of the AC@N-GA catalyst was characterized by the $N_2$ adsorption/desorption technique. The typical type-IV isotherm (Fig. 2c) indicates the presence of a mesoporous structure.[23–25] The surface area of AC@N-GA was determined to be 541.25 $m^2$ $g^{-1}$, which is much higher than that of previous graphene–aerogel based catalysts.[15,16] Pore size distribution simulated according to the Barret–Joyner–Halenda (BJH)

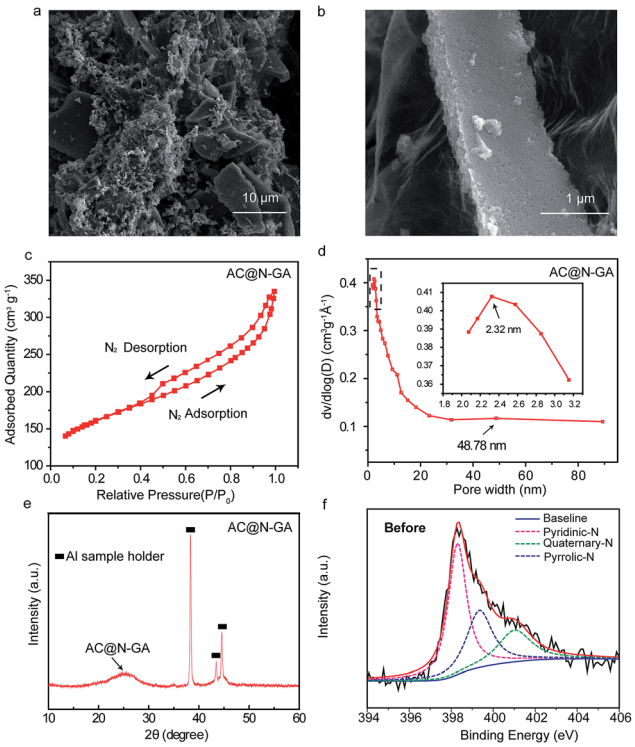


Fig. 2 (a) Low-magnified and (b) high-magnified SEM images of AC@N-GA. (c) Nitrogen adsorption/desorption isotherms and (d) pore size distribution. The inset shows the micropore distribution of the catalyst. (e) XRD pattern and (f) N 1s XPS spectra of AC@N-GA.

adsorption model is depicted in Fig. 2d. Clearly, the AC@N-GA catalyst contains micro-pores with a dominating pore width of around 2.32 nm, possibly from the microporous structure of AC. Altogether, AC@N-GA is a three-dimensional catalyst full of mesopores and micropores. Furthermore, X-ray photoelectric spectroscopy (XPS) (Fig. 2f and S2 in the ESI†) shows that the nitrogen content of AC@N-GA is 5.2%. The high-resolution N 1s peak (Fig. 2f) can be de-convoluted into several synthetic peaks associated with pyridinic-N (398.5 eV), pyrrolic-N (400.1 eV) and quarternary-N (400.8 eV).[26] The existence of these N-functional groups is beneficial for achieving excellent catalytic performance, which will be discussed in the following section.

To evaluate the catalytic performance of the as-prepared AC@N-GA catalyst, the RRDE measurement was carried out at different rotation speeds (400, 625, 900, 1225, 1600, 2025, and 2500 rpm). Fig. 3a presents the RRDE voltammograms collected at various rotating speeds. As shown in Fig. 3b, the ring current ($I_R$) is about one order of magnitude lower than the disc current ($I_D$) during the scanning process, indicating that peroxide species were rarely produced during the ORR process and a majority of oxygen was catalyzed to $OH^-$ by the AC@N-GA catalyst. Besides, the onset potential is about 0.92 V *vs.* reversible hydrogen electrode (RHE) at a rotation speed of 1600 rpm (Fig. 3c).

To further evaluate the catalytic performance of AC@N-GA, we have calculated the number of transferred electrons ($n$) based on the following formula:

$$n = \frac{4I_D}{\left(I_D + \frac{I_R}{N}\right)} \quad (1)$$

where $N$ is the collection efficiency (37%).[27] At a high rotating speed (1600 rpm), $n$ reaches 3.95 within the potential range spanning from 1.0 V to 0.75 V (Fig. 3d), which is comparable to other noble metal-based ORR catalysts.[15,16,28] The large number of transferred electrons under the steady state suggests that a four-electron pathway is the dominated process for the ORR. The yield of peroxide was calculated by the following formula:

$$\%(H_2O_2) = 200 \times \frac{I_R/N}{(I_D + I_R/N)} \quad (2)$$

The total percentage of $H_2O_2$ generated is 4.5% within the potential below 0.6 V *vs.* RHE, which is substantially lower than other graphene-based catalysts including GA-supported $Fe_3O_4$,[15] graphitic C–N dots on graphene[29] and heteroatom doped graphene nanosheets.[30] It means $O_2$ could be mainly converted to $OH^-$ rather than $H_2O_2$ (two-electron pathway). Therefore, AC@N-GA is a superior ORR catalyst and could be an excellent air-cathode for μMFCs. We ascribed the superior performance to the presence of the abundant meso-/micro-pores and the surface N-functional groups. On one hand, previous experimental results have demonstrated that synthesis of structures with high porosity is one of the key factors for an efficient carbonaceous ORR catalyst.[31] The pores could facilitate the transfer of both reactants and products for ORR (*i.e.*, $O_2$, $H^+$ and $H_2O$) and render an ultrahigh surface area that can enhance the reaction sites. On the other hand, the N-functional groups could serve as the active ORR catalytic sites. Guo *et al.* recently stated that the carbon atoms next to pyridinic N were active sites for ORR.[32] Graphitic N atoms can lower the electron density on the adjacent C atoms, and facilitate the electron transfer from C to N atoms.[33] The aforementioned conclusions are consistent with the previous studies that the mono- or multi-doped graphene materials, such as nitrogen-doped graphene/CNT/$Co_3O_4$,[34] heteroatom-doped graphene nanosheet,[30] polyaniline (PANI)/graphene and polypyrrole (Ppy)/graphene composites,[33] could achieve excellent ORR catalytic performance.

In order to characterize the practical potential of the AC@N-GA, a sandwich-configured μMFC device without the ion-exchange membrane was constructed using the AC@N-GA and rGO@Ni as the bio-anode and air-cathode, respectively, with a PMMA chamber as the micro-channel (Experimental). We choose rGO@Ni as the bio-anode because our previous study demonstrated that its large accessible surface area was favourable for the growth of a large amount of bacteria and fast mass transfer.[19] The device was then inoculated by a MFC that contained exoelectrogen suspension in a continuous-flow mode. Fig. S5a, ESI† shows the profile of voltage dependence on the inoculation time across a fixed external resistor. As shown in the figure, a lag period is initially observed and then followed by a drastic increase of the voltage output. After around 26 hours of inoculation, the maximum voltage output of 0.21 V is reached as the bacteria have successfully grown on rGO@Ni. However, the voltage soon begins to decrease in the next 8 hours before stabilizing at around 0.12 V. We ascribe such voltage decay to the bacterial growth on the surface of the air-cathode (Fig. S3, ESI†).[35] Though the bacteria were mainly grown on the solution side of the air-cathode, the bacteria and their metabolic products could clog the diffusion channels for protons and water

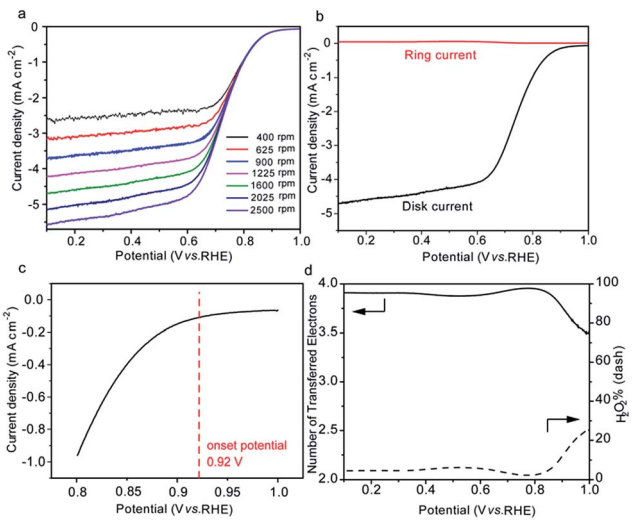


Fig. 3 (a) Various RRDE curves of AC@N-GA collected in an $O_2$-saturated 0.1 M KOH aqueous electrolyte; (b) disk and ring current–potential ($I$–$V$) curves at a rotation speed of 1600 rpm; (c) the onset potential at 1600 rpm; (d) a plot of the number of transferred electrons ($n$) and generated $H_2O_2$ percentage (%) as a function of potential at 1600 rpm.

 

from the solution side. These two components are crucial for the ORR reactions happening at the air side of the cathode and hence, sluggish transport of these components leads to obvious voltage decay. Besides, water evaporation and proton transferring from the anode side may also trigger the decay of the cell performance.[36,37] SEM images of the bacteria-inoculated rGO@Ni were taken to confirm the bacterial colonization. Compared with the plain rGO@Ni (Fig. S4, ESI†), the bio-anode surface is covered by a continuous biofilm consisting of rod-shaped bacterial cells after operation for two days (Fig. S5b, ESI†). The large amount of bacteria on the rGO@Ni is expected to guarantee a high bio-electricity generation.

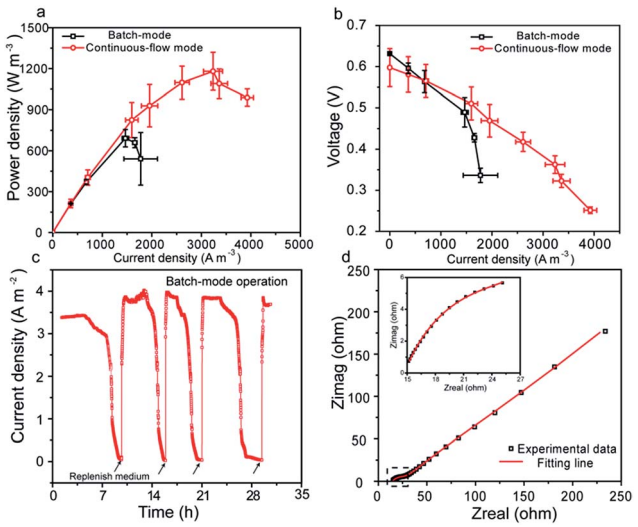


Fig. 4 (a) Volumetric power density and (b) polarization curves (batch-mode and continuous-flow mode). The error bars represent the standard deviation collected in triplicate. (c) Current density *vs.* time plot of the μMFC operated in a batch-mode with an external resistance of 5000 Ω. (d) Nyquist plot of the μMFC with an external resistance of 2000 Ω with a perturbation of 10 mV. The black squares are experimental values and the red curve is a fitting line. The inset shows the enlarged view of the indicated square region.

Power density curves and polarization curves of our μMFC were measured by recording the voltages generated with various external resistors. The cell performance under two operational modes (batch-mode and continuous-flow mode) was investigated and compared. The μMFC delivers a maximum volumetric power density of 690.2 ± 62.3 W $m^{-3}$ (batch-mode) or 1181.4 ± 135.6 W $m^{-3}$ (continuous-flow mode). The output current density at the peak power density is around 1470.2 ± 70.7 A $m^{-3}$ at the batch-mode and 3238.7 ± 178.8 A $m^{-3}$ in the continuous-flow mode (Fig. 4a). A similar open-circuit potential (OCP) of 0.59 ± 0.04 V is obtained in both cases as shown in polarization curves (Fig. 4b). Table 1 summarizes the state-of-the-art performance of μMFCs with similar configurations. Comparing with the previous studies, the practicability and capital efficiency of the μMFC device in the present study have been largely optimized because of its membrane-free architecture and low cost of the synthesized catalyst (<$2 per g).[22] The power density is even close to an enzyme-catalyzed fuel cell with a much smaller working volume (3.75 μL).[38] To our knowledge, the performance achieved by our μMFC in two operation modes are the highest among all air-cathode μMFCs and microfluidic glucose fuel cells with similar configurations. Significantly, the power outputs are capable of meeting the power demands of some niche electronics, including implanted bio-electronics,[39] *in vitro* diagnostic systems[40] and high-resolution microbial activity detectors.[41] We ascribe the excellent power output to densely-packed bacterial colonization on the bio-anode and nearly four-electron ORR pathway that occurred on the air-cathode.

Catalytic activity characterization of the AC@N-GA anode discussed in the previous sections has proved the superior performance of the anode side. To figure out the contribution of the rGO@Ni cathode to the performance of our μMFC, we have fabricated a μMFC with an identical chamber size using commercial Pt/C-coated carbon cloth and rGO@Ni as the air-cathode and bio-anode, respectively. As shown in Fig. S6(a) in the ESI,† this μMFC delivered a maximum power density of 1159.1 W $m^{-3}$ at a current density of 3217.0 A $m^{-3}$, very close to

Table 1 Comparison of cell performance generated in air-breathing μMFCs and microfluidic glucose biofuel cells[e]

| Anode | Cathode | Catalysts | Separator | Bacteria/nutrient | Volume (μL) | OCP (V) | MVPD (W $m^{-3}$) | Ref. |
|---|---|---|---|---|---|---|---|---|
| rGO@Ni | Ni foam | AC@N-GA | — | Mixed bacteria/acetate | 50 | 0.59 ± 0.04 | 1181.4 ± 135.6[a] | Present study |
| rGO@Ni | Ni foam | AC@N-GA | — | Mixed bacteria/acetate | 50 | 0.62 ± 0.01 | 690.2 ± 62.3[b] | Present study |
| Ni | CC | Pt | — | *Escherichia coli*/NB | 50 | 0.459 | 104 ± 4 | 39 |
| Ni | CC | Pt | — | *Escherichia coli*/glucose | 50 | ~0.4[d] | 52 ± 2 | 39 |
| Au | NA | Pt | PEM | *Shewanella* sp./lactate | 25 | ~0.91[d] | 14.6[c] | 42 |
| Carbon nanotube | CC | Pt | — | Mixed bacteria/acetate | 75 | — | 6.70 | 43 |
| Graphene on copper | CC | Pt | — | Mixed bacteria/acetate | 25 | — | 8 | 44 |
| Gold | Gold | — | PEM | *S. cerevisiae*/glucose | 16 | 0.488 | 30[c] | 45 |
| Enzyme-modified gold | PDMS-coated Pt | Pt | — | Poly-L-lysine/glucose | ~10[d] | 0.55 | 111.6[c] | 46 |
| Gold | Gold | Laccase | — | Enzyme glucose oxidase/glucose | 3.75[c] | 0.55 | 1466.7[c] | 38 |

[a] Continuous-flow mode. [b] Batch-mode. [c] Calculations based on reported data. [d] Evaluations based on reported figures. [e] Abbreviations: MVPD: maximum volumetric power density; CC: carbon cloth; PEM: proton exchange membrane; NB: nutrient broth.

our best values (1181.4 ± 135.6 W $m^{-3}$@3238.7 ± 100 A $m^{-3}$). Furthermore, the RRDE test for the Pt/C catalyst (mass loading: 80 μg $mg^{-2}$) exhibited that the limiting current and onset potential were similar to those of AC@N-GA (Fig. S6(b), ESI†) and is substantially better than that of other μMFCs with the Pt/C cathode.[39,42–46] These results have unequivocally proved the superior performance of the rGO@Ni anode. Combining with other characterization techniques showing that the AC@N-GA is an excellent ORR catalyst, we are confident that the exceptional performance of our μMFC should be due to both the cathode and anode. In addition, the μMFC also displayed stable performance. Fig. 4c shows the current response of the μMFC device during four feeding cycles operated in a batch-mode. Pronounced current generation is observed at the beginning of every feeding cycle and it is stable for more than 2 hours. Replenishing the electrolyte results in the complete recovery of bio-electricity, further suggesting that the performance is quite stable.

Electrochemical impedance spectroscopy (EIS) was carried out to further characterize the internal resistance of the μMFC. A semicircle (middle-frequency domain) followed by a straight line (mass transfer-control region) is observed in the Nyquist plot as shown in Fig. 4d. By fitting the Nyquist plot with an equivalent electric circuit (Fig. S7, ESI†), the values of ohmic resistance ($R_\Omega$), charge transfer resistance ($R_{CT}$) and diffusion resistance ($R_D$) were obtained and summarized in Table S1, ESI.† As shown in the table, $R_\Omega$ (14.6 Ω) has a small contribution to the total internal resistance (~700 Ω). Correspondingly, $R_{CT}$ (458.5 Ω) and $R_D$ (227.5 Ω) dominate the total internal resistance. This result could be due to the relatively limited oxygen transport at the cathode. The bacterial adhesion or other organic matter attachment at the cathode (Fig. S3, ESI†) may clog the pores and lower the oxygen transfer efficiency.[35] Nevertheless, the total internal resistance of ~700 Ω is substantially lower than the values of previous reports based on similar dimensions.[5,6,21,39] The low internal resistance is an insurance to achieve the superior μMFC performance and demonstrates the feasibility of the μMFC design.

In order to evaluate the long term stability of the AC@N-GA, we have incorporated it into a μMFC and operated for 20 days. We then disassembled the device, cleaned the AC@N-GA and performed both XPS (Fig. S8, ESI†) and the RRDE test (Fig. S9, ESI†) to probe the change of N content and catalytic activity, respectively. As shown in Table S2 (in the ESI†), the N content of the AC@N-GA after the test is 5.49 at%, which is slightly higher than that of the as-prepared AC@N-GA (5.22 at%). Such a small discrepancy is believed to stem from the biomass (bacteria or their metabolic products) attached on the catalyst surface. Moreover, the same types of N-functional groups including pyridinic-N, quaternary-N and pyrrolic-N are observed before and after the stability test. The XPS results confirm the stable composition of the AC@N-GA cathode.

RRDE tests with various rotation speeds have been performed to confirm the catalytic performance stability, and the results are depicted in Fig. S9(a), ESI.† The limiting currents at various rotating speeds are nearly identical to those of the as-prepared catalyst. An onset potential of +0.82 V *vs.* RHE is identified from the RRDE spectrum at 1600 rpm. This onset potential is slightly decreased compared to that of the as-prepared catalyst (+0.92 V *vs.* RHE). (Fig. S9(b), ESI†) The decayed onset potential may be due to the biomass coating as illustrated by the XPS test and SEM images (Fig. S5(b), ESI†). This bio-coating hinders reactant transport and impacts the catalytic performance of ORR catalysts.

## Conclusions

In summary, we have successfully fabricated the AC@N-GA composite material as an inexpensive and superior ORR catalyst. Owing to the ultrahigh surface area and the existence of N-functional groups, the AC@N-GA displays a very high number of transferred electrons (3.9) and an ultra-small percentage of generated $H_2O_2$ (4.5%). A low-cost, membrane-free μMFC device with the AC@N-GA as the air-cathode and rGO@Ni as the bio-anode exhibits superior power densities of 1181.4 ± 135.6 W $m^{-3}$ (continuous-flow mode) and 690.2 ± 62.3 W $m^{-3}$ (batch-mode), which are substantially higher than those of other μMFCs with a similar configuration. The excellent ORR catalytic performance of AC@N-GA and the 3D hierarchically porous structure of rGO@Ni that enables high bacterial community uptake are believed to be the two crucial factors determining the remarkable performance. We believe the successful fabrication of the AC@N-GA could significantly advance the μMFC technology towards large-scale manufacturing of commercial electronic products including portable power generators and sensors.

## Acknowledgements

This work is also supported by the National Natural Science Funds for Distinguished Young Scholar (No. 51325602), National Natural Science Foundation of China (No. 51376203, No. 51276208), Fundamental Research Funds for the Central Universities (No. CDJZR14145502) and Overseas, and the Hong Kong & Macao Scholars Collaborated Research Fund (No. 51428601). Y. L. thanks the financial support from NSF (IIP-1550327). Y. Y. thanks the China Scholarship Council for financial support. T. L. thanks the financial support from the Chancellor's Dissertation Year Fellowship awarded by UC Santa Cruz. We also acknowledge the kind help offered by Wei Yang, Rui Wu and Zeyu Fan.

## Notes and references

1 B. E. Logan, B. Hamelers, R. Rozendal, U. Schröder, J. Keller, S. Freguia, P. Aelterman, W. Verstraete and K. Rabaey, *Environ. Sci. Technol.*, 2006, **40**, 5181–5192.
2 D. R. Bond, D. E. Holmes, L. M. Tender and D. R. Lovley, *Science*, 2002, **295**, 483–485.
3 E. Kjeang, N. Djilali and D. Sinton, *J. Power Sources*, 2009, **186**, 353–369.
4 J. W. Lee and E. Kjeang, *J. Power Sources*, 2013, **242**, 472–477.
5 Y. Yang, D. Ye, J. Li, X. Zhu, Q. Liao and B. Zhang, *Int. J. Hydrogen Energy*, 2015, **40**, 11983–11988.

 

6 Y. Yang, D. Ye, Q. Liao, P. Zhang, X. Zhu, J. Li and Q. Fu, *Biosens. Bioelectron.*, 2016, **79**, 406–410.
7 D. Davila, J. P. Esquivel, N. Sabate and J. Mas, *Biosens. Bioelectron.*, 2011, **26**, 2426–2430.
8 J. Kim, J. Hwan Ko, J. Lee, M. Jun Kim and D. Byun, *Appl. Phys. Lett.*, 2014, **104**, 223702.
9 J. E. Mink, J. P. Rojas, B. E. Logan and M. M. Hussain, *Nano Lett.*, 2012, **12**, 791–795.
10 J. E. Mink and M. M. Hussain, *ACS Nano*, 2013, **7**, 6921–6927.
11 H. Ren, H. Tian, C. L. Gardner, T.-L. Ren and J. Chae, *Nanoscale*, 2016, **8**, 3539–3547.
12 H. Yuan and Z. He, *Nanoscale*, 2015, **7**, 7022–7029.
13 Z. He, J. Liu, Y. Qiao, C. M. Li and T. T. Tan, *Nano Lett.*, 2012, **12**, 4738–4741.
14 H. Dong, H. Yu, H. Yu, N. Gao and X. Wang, *J. Power Sources*, 2013, **232**, 132–138.
15 Z.-S. Wu, S. Yang, Y. Sun, K. Parvez, X. Feng and K. Müllen, *J. Am. Chem. Soc.*, 2012, **134**, 9082–9085.
16 H. Yin, C. Zhang, F. Liu and Y. Hou, *Adv. Funct. Mater.*, 2014, **24**, 2930–2937.
17 C. Huang, C. Li and G. Shi, *Energy Environ. Sci.*, 2012, **5**, 8848.
18 W. S. Hummers Jr and R. E. Offeman, *J. Am. Chem. Soc.*, 1958, **80**, 1339.
19 H. Wang, G. Wang, Y. Ling, F. Qian, Y. Song, X. Lu, S. Chen, Y. Tong and Y. Li, *Nanoscale*, 2013, **5**, 10283–10290.
20 J. Xuan, D. Leung, H. Wang, M. K. Leung, B. Wang and M. Ni, *Appl. Energy*, 2013, **104**, 400–407.
21 D. Ye, Y. Yang, J. Li, X. Zhu, Q. Liao, B. Deng and R. Chen, *Int. J. Hydrogen Energy*, 2013, **38**, 15710–15715.
22 Y. Yang, T. Liu, X. Zhu, F. Zhang, D. Ye, Q. Liao and Y. Li, *Adv. Sci.*, 2016, **3**, 1600097.
23 X. Zhang, Z. Sui, B. Xu, S. Yue, Y. Luo, W. Zhan and B. Liu, *J. Mater. Chem.*, 2011, **21**, 6494–6497.
24 M. A. Worsley, P. J. Pauzauskie, T. Y. Olson, J. Biener, J. H. Satcher Jr and T. F. Baumann, *J. Am. Chem. Soc.*, 2010, **132**, 14067–14069.
25 Z. Sui, Q. Meng, X. Zhang, R. Ma and B. Cao, *J. Mater. Chem.*, 2012, **22**, 8767–8771.
26 P. Chen, J.-J. Yang, S.-S. Li, Z. Wang, T.-Y. Xiao, Y.-H. Qian and S.-H. Yu, *Nano Energy*, 2013, **2**, 249–256.
27 K. Liu, Y. Song and S. Chen, *Nanoscale*, 2015, **7**, 1224–1232.
28 Y. Liang, Y. Li, H. Wang, J. Zhou, J. Wang, T. Regier and H. Dai, *Nat. Mater.*, 2011, **10**, 780–786.
29 X. Wang, L. Wang, F. Zhao, C. Hu, Y. Zhao, Z. Zhang, S. Chen, G. Shi and L. Qu, *Nanoscale*, 2015, **7**, 3035–3042.
30 M. Park, T. Lee and B.-S. Kim, *Nanoscale*, 2013, **5**, 12255–12260.
31 C. M. Parlett, K. Wilson and A. F. Lee, *Chem. Soc. Rev.*, 2013, **42**, 3876–3893.
32 D. Guo, R. Shibuya, C. Akiba, S. Saji, T. Kondo and J. Nakamura, *Science*, 2016, **351**, 361–365.
33 L. Lai, J. R. Potts, D. Zhan, L. Wang, C. K. Poh, C. Tang, H. Gong, Z. Shen, J. Lin and R. S. Ruoff, *Energy Environ. Sci.*, 2012, **5**, 7936–7942.
34 S.-S. Li, H.-P. Cong, P. Wang and S.-H. Yu, *Nanoscale*, 2014, **6**, 7534–7541.
35 F. Zhang, D. Pant and B. E. Logan, *Biosens. Bioelectron.*, 2011, **30**, 49–55.
36 S. Yang, B. Jia and H. Liu, *Bioresour. Technol.*, 2009, **100**, 1197–1202.
37 P. Cristiani, M. Carvalho, E. Guerrini, M. Daghio, C. Santoro and B. Li, *Bioelectrochemistry*, 2013, **92**, 6–13.
38 A. Zebda, L. Renaud, M. Cretin, F. Pichot, C. Innocent, R. Ferrigno and S. Tingry, *Electrochem. Commun.*, 2009, **11**, 592–595.
39 M. M. Mardanpour and S. Yaghmaei, *Biosens. Bioelectron.*, 2016, **79**, 327–333.
40 A. Fraiwan, S. Mukherjee, S. Sundermier, H. S. Lee and S. Choi, *Biosens. Bioelectron.*, 2013, **49**, 410–414.
41 H. Hou, L. Li, Y. Cho, P. de Figueiredo and A. Han, *PLoS One*, 2009, **4**, e6570.
42 Y. P. Chen, Y. Zhao, K. Q. Qiu, J. Chu, R. Lu, M. Sun, X. W. Liu, G. P. Sheng, H. Q. Yu, J. Chen, W. J. Li, G. Liu, Y. C. Tian and Y. Xiong, *Biosens. Bioelectron.*, 2011, **26**, 2841–2846.
43 J. E. Mink and M. M. Hussain, *ACS Nano*, 2013, **7**, 6921–6927.
44 J. E. Mink, R. M. Qaisi, B. E. Logan and M. M. Hussain, *NPG Asia Mater.*, 2014, **6**, e89.
45 C. P. B. Siu and C. Mu, *J. Microelectromech. Syst.*, 2008, **17**, 1329–1341.
46 M. Togo, A. Takamura, T. Asai, H. Kaji and M. Nishizawa, *Electrochim. Acta*, 2007, **52**, 4669–4674.